

# Experimental Highlights of the RHIC Program

Patricia Fachini

*Brookhaven National Laboratory, P.O. BOX 5000, Upton, NY, USA.*

**Abstract.** Experimental highlights of the RHIC program are reviewed.

## INTRODUCTION

Relativistic heavy-ion collisions provide a unique environment to study matter under extreme conditions of high temperature and energy density. RHIC (Relativistic Heavy Ion Collider) at the Brookhaven National Laboratory in Upton, NY provides us with such collisions. Since the beginning of the RHIC operation in the year 2000, RHIC has provided us not only with Au+Au collisions at the top energy of  $\sqrt{s_{NN}} = 200$  GeV, but also at 62 GeV. RHIC has also provided collisions of lighter systems such as Cu+Cu at  $\sqrt{s_{NN}} = 200, 62,$  and 22.5 GeV, and finally the  $p + p$  and  $d + \text{Au}$  collisions at  $\sqrt{s_{NN}} = 200$  GeV that were used as references.

The amount of data obtained so far is as overwhelming as the results. I will try to summarize where we are, with RHIC RUNV just about to start.

## ELLIPTIC FLOW

In non-central collisions the initial spatial anisotropy is transformed into an anisotropy in momentum-space if sufficient interactions occur among the constituents within the system. Once the system has expanded enough to quench the spatial anisotropy, further development of momentum anisotropy ceases. This self-quenching process happens quickly, so elliptic flow is primarily sensitive to the early stages of the collisions [1].

## Hydrodynamics

The elliptic flow  $v_2$  as a function of  $p_t$  for  $K_S^0, \Lambda, \phi, \Xi,$  and  $\Omega$  is depicted in Fig. 1 [2, 3]. The  $\phi, \Xi,$  and  $\Omega$  have low hadronic cross-sections, therefore the large  $v_2$  observed suggest that the elliptic flow is built up in the partonic stage. The expected range of  $v_2$  from hydrodynamic calculations is also shown in Fig. 1. A more detailed comparison can be seen in Fig. 2 (left panel), where the mass dependence hydrodynamic results [1] are compared to the  $v_2$  measurements of  $\pi, K, p,$  and  $\Lambda$  [4]. Hydrodynamics describes well the mass dependence observed in the data that is characteristic of a common flow velocity. Since an ideal hydrodynamic fluid is a thermalized system with a zero mean

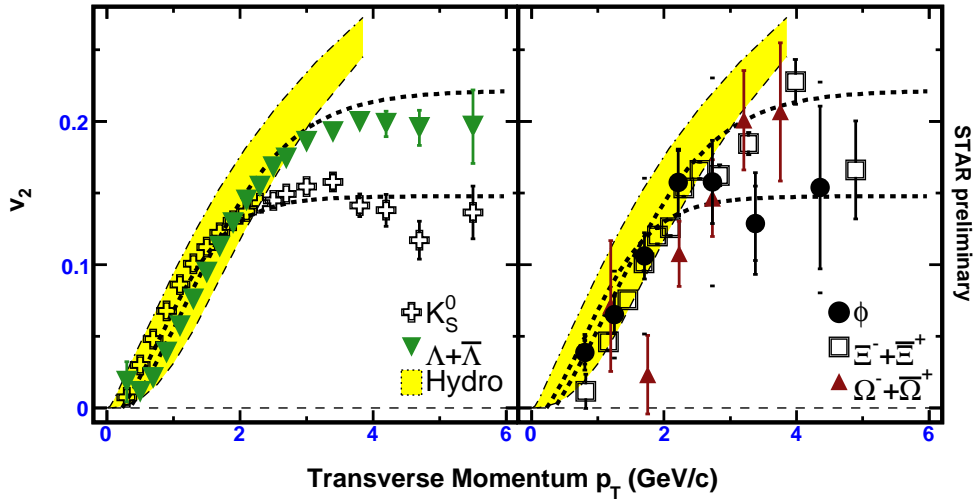


**FIGURE 1.** Azimuthal anisotropy  $v_2$  for strange (left panel) and multi-strange (right panel) hadrons in minimum bias Au+Au collisions [2]. Data measured by STAR. The dashed lines show a common fit to the  $K_S^0$  and  $\Lambda + \bar{\Lambda}$  data [5]. The shaded areas are hydrodynamic calculations [1]

free path that yields to the maximum possible  $v_2$ , the good agreement between the measured  $v_2$  and the hydro results [1] suggests thermalization in heavy-ion collisions at RHIC.

## Constituent Quark Scaling

While hydrodynamic calculations keep increasing as a function of  $p_T$ , the measured  $v_2$  saturate at  $p_T > 2$  GeV/c [2]. The saturation value for mesons is about 2/3 of that for baryons. This separation pattern holds for  $\pi, K, \Lambda$ , and  $\Xi$ , and seems to hold for  $\phi$  and  $\Omega$  [3, 6]. This result and the baryon-meson splitting of the high  $p_T$  suppression pattern [7] suggest the relevance of the constituent quark degrees of freedom in the intermediate  $p_T$  region [8].  $v_2$  scaled by the number of valence quarks  $n$  as a function of  $p_T/n$  is depicted in Fig. 2 (right panel). The lower panel of Fig. 2 (right panel) displays the ratio between the measurements and a polynomial fit to all the data. At low  $p_T/n$  the observed deviations from the fit follow a mass ordering which is expected from hydrodynamics. At higher  $p_T$ , all  $v_2/n$  measurements are reasonably close to unity showing the constituent quark scaling.

## FREEZE-OUT PROPERTIES

The measured particle spectra and yields [9] and event-by-event  $\langle p_T \rangle$  fluctuations [10] indicate a nearly chemically and kinetically equilibrated system at the final freeze-out stage.

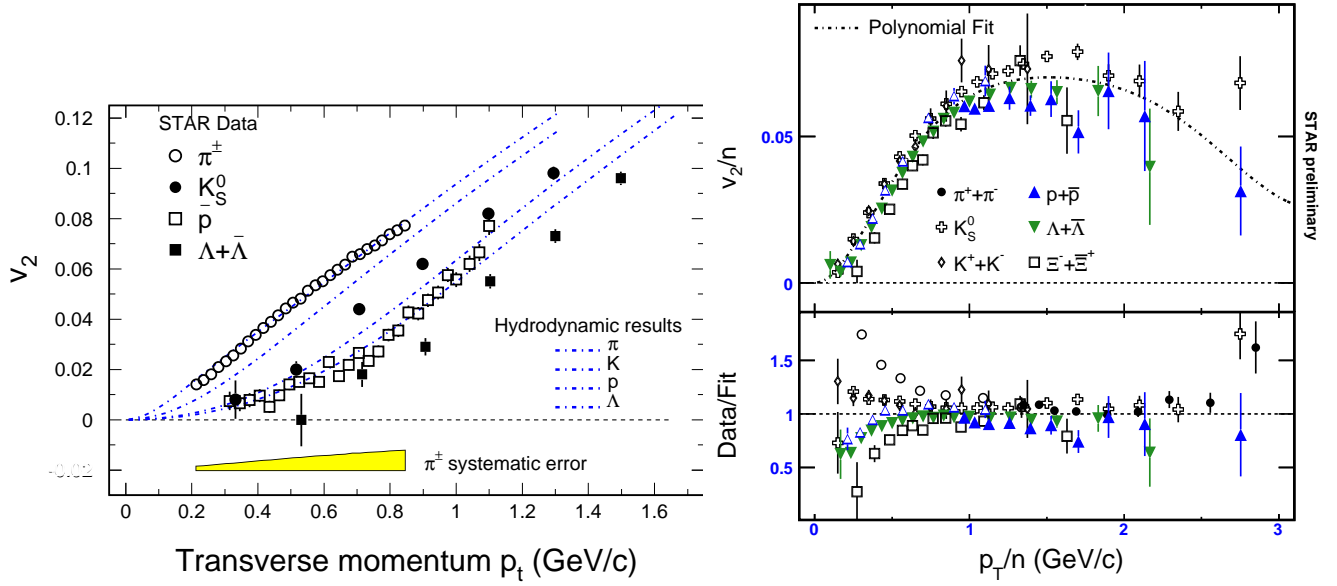


**FIGURE 2.** Left panel:  $v_2$  as a function of  $p_T$  from minimum bias Au+Au collisions [4] measured by STAR. The dotted-dashed lines are hydrodynamic calculations using an equation of state (EOS) with a first-order hadron-quark-gluon plasma phase transition [1]. The description of the data worsens if a hadronic EOS is used [1]. Right panel: Measurements by STAR of the scaled  $v_2(p_T/n)/n$  for identified hadrons (upper panel) and the ratio between the measurements and a polynomial fit through all data points (lower panel) except the pions for  $\sqrt{s_{NN}} = 200$  GeV minimum bias Au+Au collisions [2].

## Chemical and Kinetic Freeze-out Parameters

STAR has now measured hadron distributions at  $\sqrt{s_{NN}} = 200$  and 62 GeV [11, 12]. Chemical freeze-out properties were extracted from stable particle ratios within the thermal model [15]. The extracted chemical freeze-out temperature  $T_{ch}$  and the strangeness suppression factor  $\gamma_s$  are depicted in Fig. 3. Kinetic freeze-out properties from particle  $p_T$  distributions were extracted within the blast wave model [16]. Figure 4 displays the extracted kinetic freeze-out temperature  $T_{kin}$  and the average radial flow velocity  $\langle\beta_T\rangle$ . The results at  $\sqrt{s_{NN}} = 62$  GeV are found to be qualitatively the same as those obtained at  $\sqrt{s_{NN}} = 200$  GeV and resonance decays are found to have no significant effect on the extracted kinetic freeze-out parameters [12].

$T_{ch}$  is independent of centrality.  $T_{kin}$  obtained from  $\pi$ ,  $K$ , and  $p$  decreases as a function of centrality, while the corresponding  $\langle\beta_T\rangle$  increases. This is evidence that the system expands between chemical and kinetic freeze-outs, which brings the system to a lower temperature. The constant  $T_{ch}$  suggests that hadronic scatterings from hadronization to chemical freeze-out may be negligible because they would result in a dropping  $T_{ch}$ .

$\gamma_s$  increases from  $p+p$  to peripheral and central Au+Au collisions. In central Au+Au collisions,  $\gamma_s$  is  $\sim 1$  suggesting that strangeness is saturated. The  $T_{ch}$  of  $\phi$ ,  $\Xi$ , and  $\Omega$  is higher than that of  $\pi$ ,  $K$ , and  $p$ , while the  $\langle\beta_T\rangle$  is lower. Noting that the  $\phi$ ,  $\Xi$ , and  $\Omega$  have small hadronic cross-sections, they may chemically and kinetically freeze-out at the same time.

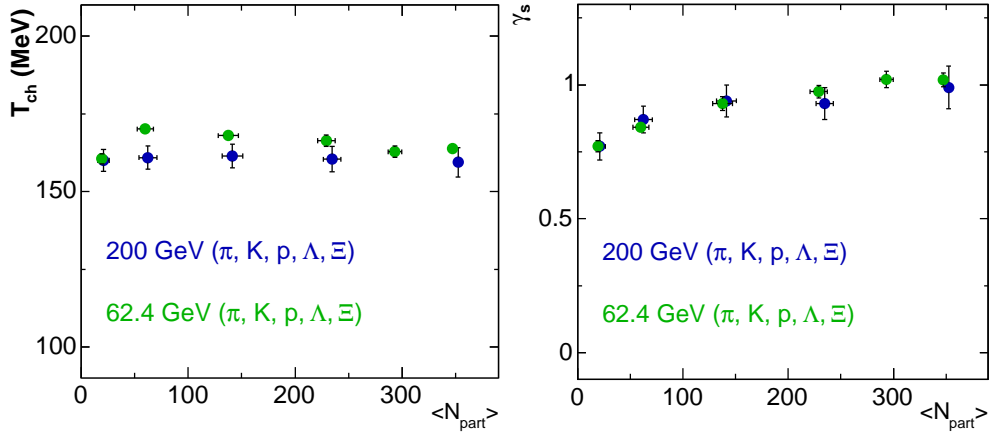


**FIGURE 3.** Left panel: Extracted chemical freeze-out temperature from stable particle ratios [11, 12]. Right panel: Extracted strangeness suppression factor from stable particle ratios [11, 12]. STAR measurements.

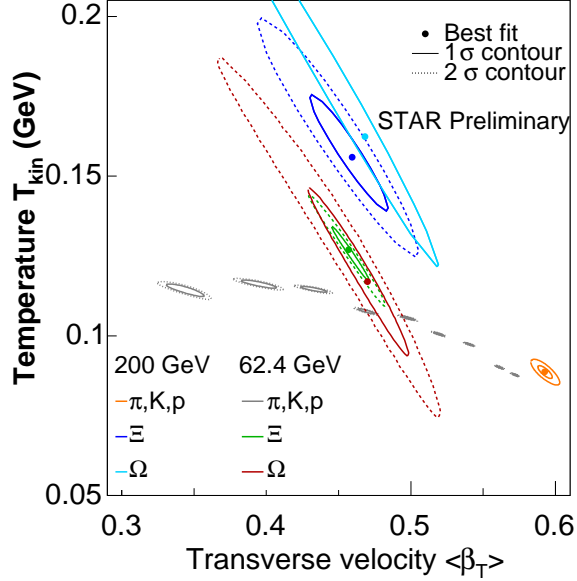


**FIGURE 4.** Extracted kinetic freeze-out temperature as a function of the average flow velocity within the blast-wave model [11, 12]. STAR measurements.

## SYSTEM SIZE DEPENDENCE

The comparison between the charged hadron pseudorapidity distributions measured by PHOBOS [13] in Cu+Cu and Au+Au with similar number of participants  $N_{part}$  is presented in Fig. 5. Both distributions are comparable within errors, showing that bulk particle production depends mainly on the number of participating nucleons. The same is true for different  $N_{part}$  and also at  $\sqrt{s_{NN}} = 62$  GeV [13]. Many other measurements from BRAHMS, PHENIX, PHOBOS, and STAR support this argument [20, 30, 13, 7].

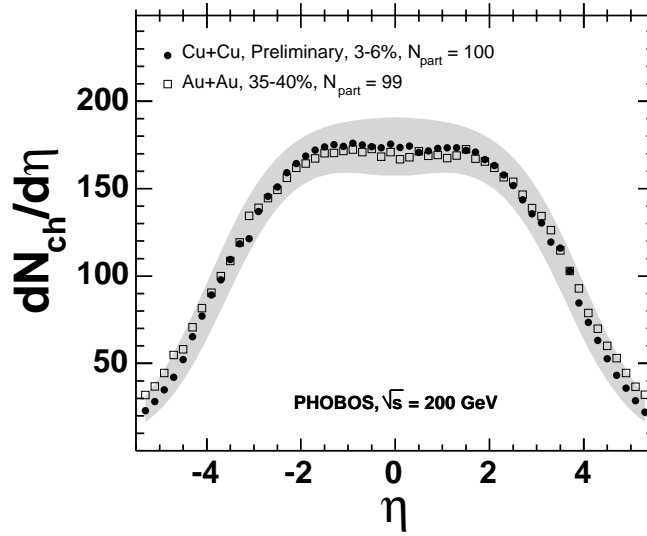


**FIGURE 5.** Charged hadron pseudorapidity measured by PHOBOS for Cu+Cu and Au+Au collisions at  $\sqrt{s_{NN}} = 200$  GeV with similar number of participants  $N_{part}$

## LOW $P_T$ HADRONS

The nuclear modification factor  $R_{AA}$  of  $\pi$  and  $p$  measured at  $y = 3.2$  by BRAHMS and  $y = 0$  by PHENIX in central Au+Au collisions does not depend on rapidity [20], suggesting that the same mechanisms is responsible for the nuclear modifications. It has been predicted [21] that the magnitude of jet quenching should depend on both the size and the density of the created absorbing medium. The averaged pion  $R_{AA}$  as a function of  $N_{part}$  for both forward rapidity and mid-rapidity are shown in Fig. 6. The average was performed in the interval  $2 < p_T < 3$  GeV/c. The mid- and forward rapidity pion suppression for the most central Au+Au collisions are found to be the same magnitude. However, the  $R_{AA}$  measured in forward rapidity shows significantly stronger rise towards peripheral collisions as compared to  $R_{AA}$  at mid-rapidity, differing on the level of 35% for  $\langle N_{part} \rangle \approx 100$ . This is consistent with the model of parton energy loss in a strongly absorbing medium [22, 23]. In this picture, at mid-rapidity, the emission is dominated by the emission from the surface which quenches the dependence of  $R_{AA}$  on the system. On the other hand, at forward rapidities, the transition from surface to volume emission can occur, which leads to a stronger dependence on the number of participants.

## INTERMEDIATE $P_T$ HADRONS

Intermediate  $p_T$  ( $p_T < 6$  GeV/c) protons behave differently than mesons at heavy-ion collisions [6]. This behavior can be seen in Fig. 7 (left panel) that depicts the ratio of  $p$  to  $\pi$  spectra measured by STAR in both central Au+Au collisions and in  $p + p$  collisions. The large enhancement of the  $p/\pi$  ratio at intermediate  $p_T$  in Au+Au collisions indicates that jet fragmentation in vacuum is not the dominant source of particle production in

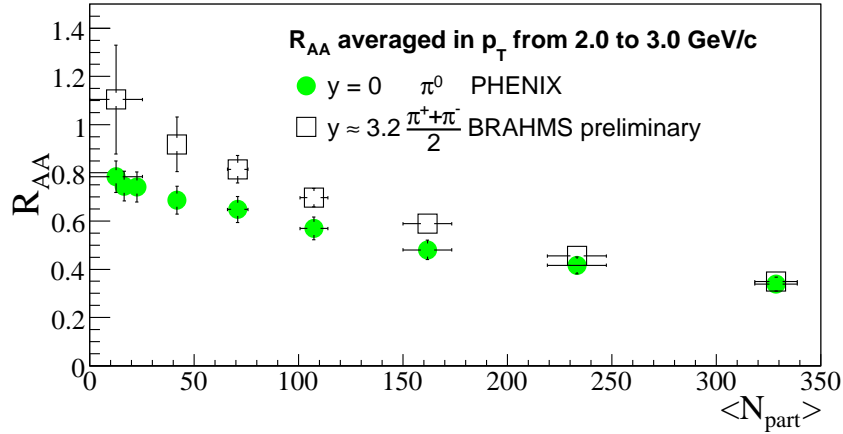


**FIGURE 6.** Averaged  $R_{AA}$  in the interval  $2.0 < p_T < 3.0$  GeV/c at mid-rapidity (PHENIX) and at forward rapidity (BRAHMS) as a function of number of participants at  $\sqrt{s_{NN}} = 200$  GeV [20]

this  $p_T$  range. An enhancement, roughly peaked at the same position, is also observed in  $R_{CP}$ , as shown in Fig. 7 (right panel). Here,  $R_{CP}$  is the ratio between central and peripheral Au+Au collisions normalized to the binary collision scaling expectation. Like  $v_2$  [2],  $R_{CP}$  also separates into baryons and mesons. The  $K^*$  [17], which is a meson with the mass close to the proton mass, follow the behavior of mesons. This proves that this separation is not due to the hadron mass. This grouping is violated in  $R_{AA}$ , where the reference is from  $p + p$  collisions rather than peripheral collisions. A strong enhancement in strange baryon  $R_{AA}$  with increasing enhancement for increasing strangeness content is observed at intermediate  $p_T$  [18]. This enhancement is depicted in Fig. 8.

## HIGH $P_T$ HADRONS

The suppression of high  $p_T$  hadrons in central Au + Au collisions was one of the unexpected and important phenomena observed at RHIC. The  $R_{AA}$  of  $\pi^0$  measured by PHENIX in central Au+Au collisions at  $\sqrt{s_{NN}} = 200$  GeV [24] is presented in Fig. 9. The suppression is quite strong ( $R_{AA} \sim 0.2$ ) and remains approximately flat up to 20 GeV/c. Partonic radiative energy loss models [25, 26, 27] reproduce this behavior well. In particular, one calculation depicted in Fig. 9 uses an average gluon average density  $dN_g/dy \sim 1200$  [25]. The  $R_{AA}$  measured by PHENIX and STAR are shown in Fig. 9 [24] and Fig. 10 [19], respectively. The difference between charged hadrons  $R_{AA}$  and the  $\pi^0$   $R_{AA}$  in the intermediate  $p_T$  region ( $p_T < 6$  GeV/c) is due to the proton contribution as observed in Fig. 10 and nicely described by recombination models. This behavior disappears for  $p_T > 6$  GeV/c and are also explained by the same recombination models [28, 29, 30].

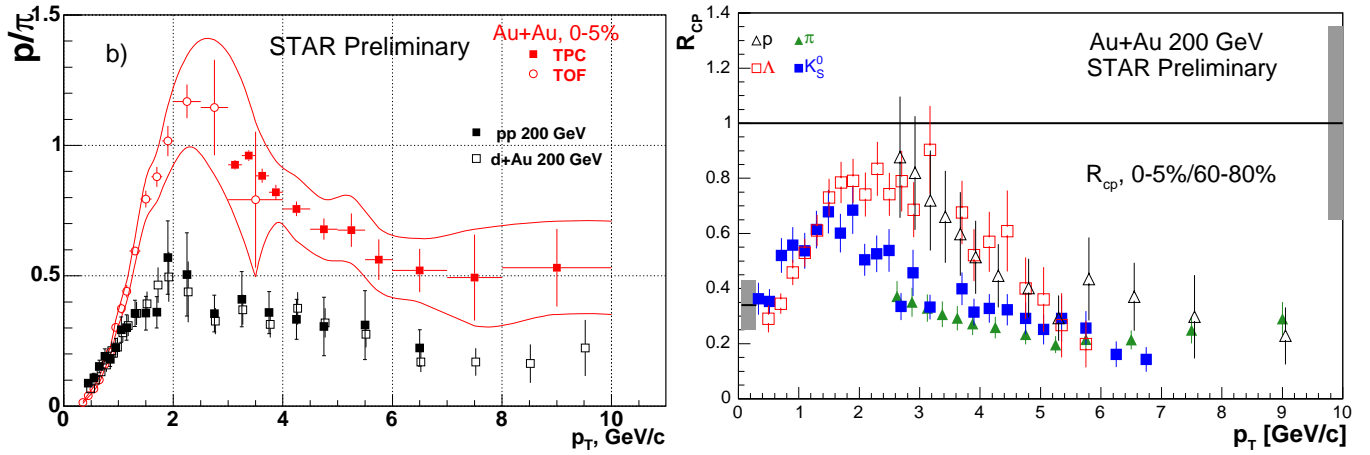


**FIGURE 7.** Left panel:  $p/\pi$  ratio measured by STAR as a function of  $p_T$  for central Au+Au (0-5%), d+Au and  $p+p$  collisions [19]. For the Au+Au measurements, the error bars are statistical only and the solid lines are the systematic uncertainties. For the d+Au and  $p+p$  measurements, the errors shown are combined statistical and systematic. Right panel:  $R_{CP}$  as a function of  $p_T$  for identified particles measured by STAR [18, 19]. Errors are statistical and systematic. Grey bands are common scale uncertainties from  $N_{binary}$ .

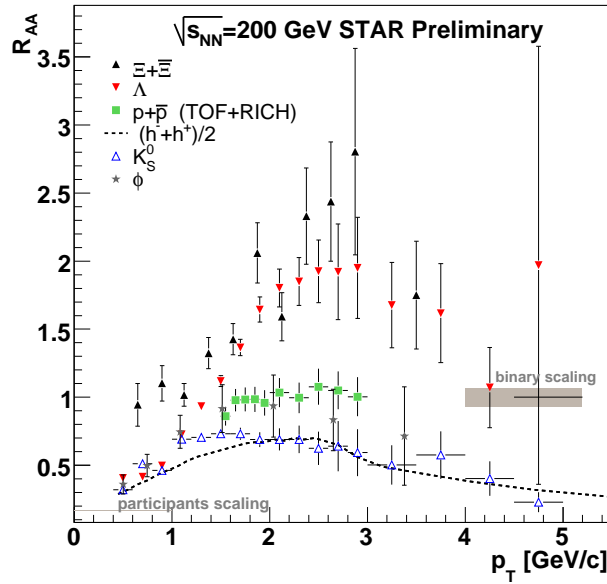


**FIGURE 8.**  $R_{AA}$  as a function of  $p_T$  for identified particles measured by STAR [18, 19]. Errors are statistical and systematic. Grey bands are common scale uncertainties from  $N_{binary}$ .

## JET CORRELATIONS

A well defined back-to-back peak that is characteristic of di-jets is observed with negligible background in Fig. 11 in both peripheral and central Au+Au collisions measured by STAR [31]. While the yield is substantially less in central Au+Au collisions, the widths

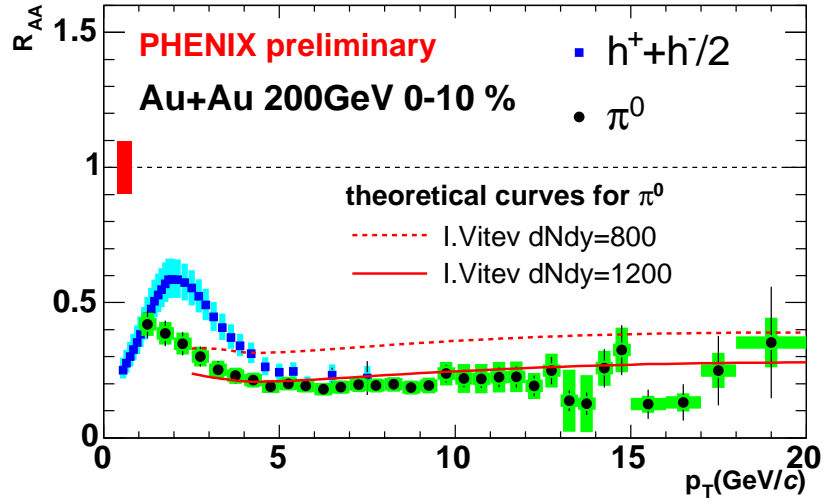


**FIGURE 9.**  $R_{AA}$  as a function of  $p_T$  of  $\pi^0$  and charged hadrons measured by PHENIX in central Au+Au collisions (0-10%) with theoretical predictions [25, 26]. The shaded areas are the systematic uncertainties.

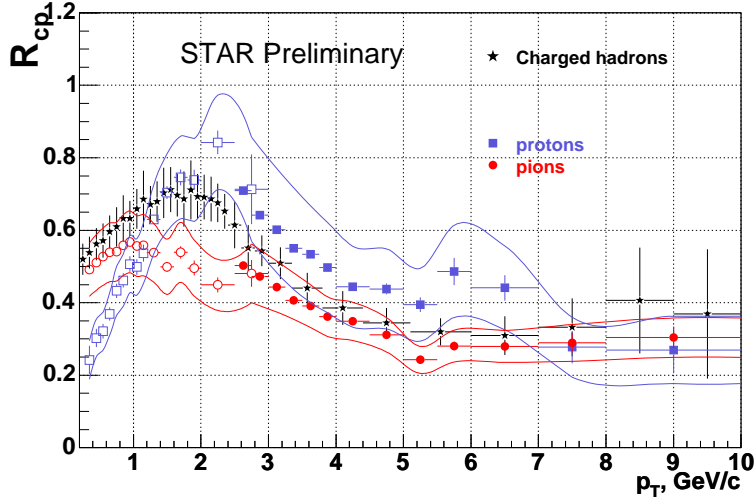


**FIGURE 10.**  $R_{CP}$  for the 5% most central collisions measured by STAR, normalized by the peripheral 60-80% collisions, as a function of  $p_T$  [19]. The bands show combined statistical and systematic errors.

of the back-to-back peaks appear to be independent of centrality. The away-side hadron triggered fragmentation functions [26] for  $d$ +Au and Au+Au collisions [31] measured by STAR as a function of  $z_T = p_T^{assoc}/p_T^{trig}$  is depicted in Fig. 12 (left panel). Fig. 12 (left panel) shows that the shape of the away-side fragmentation functions is unchanged from  $d$ +Au to central Au+Au collisions. However, the yields are reduced by a factor of  $\sim 4$  in central Au+Au collisions. Even though the shape is consistent with previous predictions in the  $z_T$  range measured, the magnitude is smaller than expected [26]. A different calculation predicted that significant energy loss should be associated with significant broadening of the away-side hadron azimuthal distribution [32], in contradiction to the



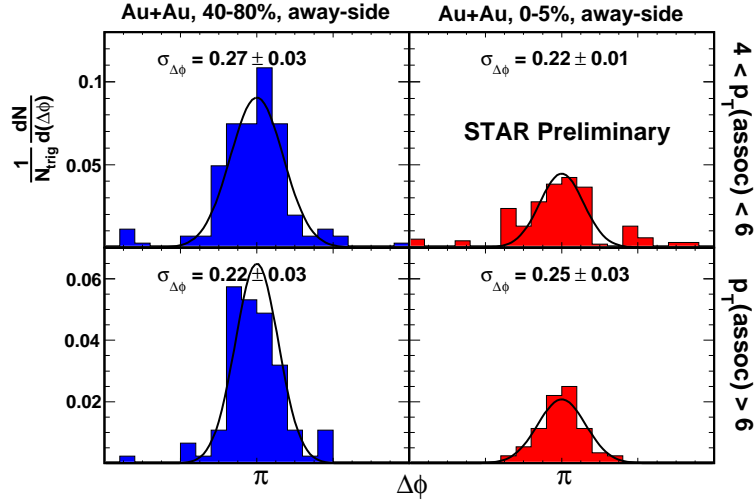


**FIGURE 11.** Azimuthal distributions of away-side charged hadrons for  $8 < p_T^{trig} < 15$  GeV/c in two different centralities at  $\sqrt{s_{NN}} = 200$  GeV Au+Au collisions. These are the total distributions, no backgrounds have been subtracted.

STAR measurements.

When low- $p_T$  associated particles are observed in central Au+Au collisions opposite a high- $p_T$  trigger particle, they are found to be significantly broadened in  $\Delta\phi$  and enhanced in number compared to  $p + p$  collisions [33]. Contrary to the maximum found in  $p + p$  and  $d + \text{Au}$  collisions, STAR measured the  $\langle p_T \rangle$  of the associated particles appears to be a minimum at  $\Delta\phi = \pi$  in central Au+Au collisions [34]. In addition, the away-side associated particle yield is flat or may have a small dip at  $\Delta\phi = \pi$  [34]. These phenomena are displayed in Fig. 12 (right panel) and have led to predictions that we may be observing jets that have been deflected by radial flow or a Mach cone effect associated with conical shock waves [35].

## HEAVY FLAVOR

The nuclear modification factor  $R_{AA}$  of non-photonic electrons measured by PHENIX [36] and STAR [7] in central Au+Au collisions is shown in Fig. 13. Both experiments observe a very strong suppression of the non-photonic electrons. The suppression has approximately the same shape and magnitude as the suppression for hadrons, which is a quite surprising result, since the massive quarks are expected to radiate much less energy than the lighter  $u$  and  $d$  quarks. It is important to confirm and complement these results with direct measurements of open charm and open bottom contributions. The first direct reconstruction of  $D$  mesons by STAR [37] is the first step in this direction, and more improvement will come with the implementation of new detectors from both PHENIX and STAR.

The  $v_2$  of non-photonic electrons as a function of  $p_T$  [36] measured by PHENIX is shown in Fig. 14 (left panel). The non-zero flow measured at  $p_T < 2$  GeV/c, where the

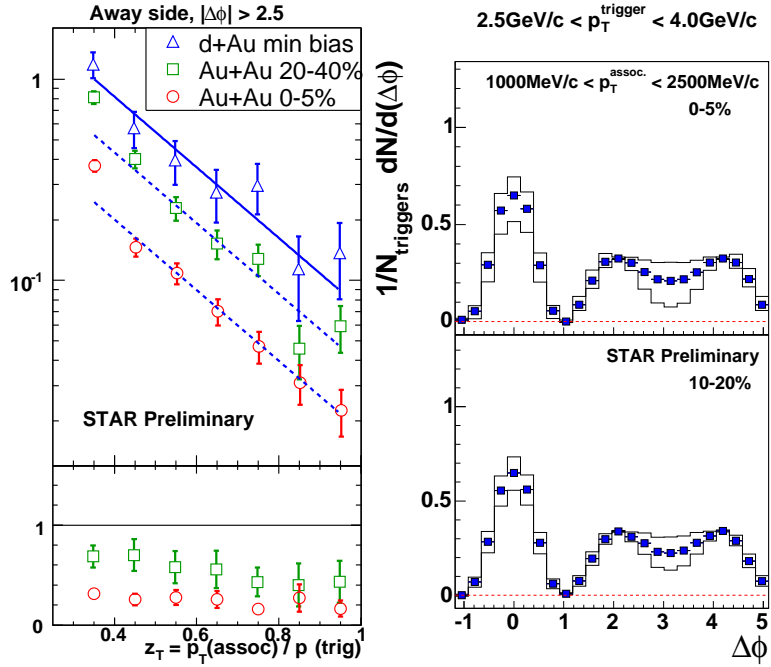


**FIGURE 12.** Left panel: Top: Hadron triggered fragmentation functions  $dN/dz_T$  for away-side charged hadrons as a function of  $z_T$  for  $8 < p_T^{trig} < 15$  GeV/c at  $\sqrt{s_{NN}} = 200$  GeV  $d+Au$  and Au+Au collisions. The solid line is an exponential fit to the  $z_T$  distribution for  $d+Au$ . The dashed lines represent the same exponential fit scaled down by factors of 0.54 and 0.25 to approximate the yields in 20-40% and 0-5% Au+Au collisions. Bottom: Ratio of the hadron triggered fragmentation functions for Au+Au/ $d+Au$ . Right panel: Azimuthal distributions of associated charged hadrons for two different centralities at  $\sqrt{s_{NN}} = 200$  GeV Au+Au collisions. The histograms indicate the systematic uncertainty bands.

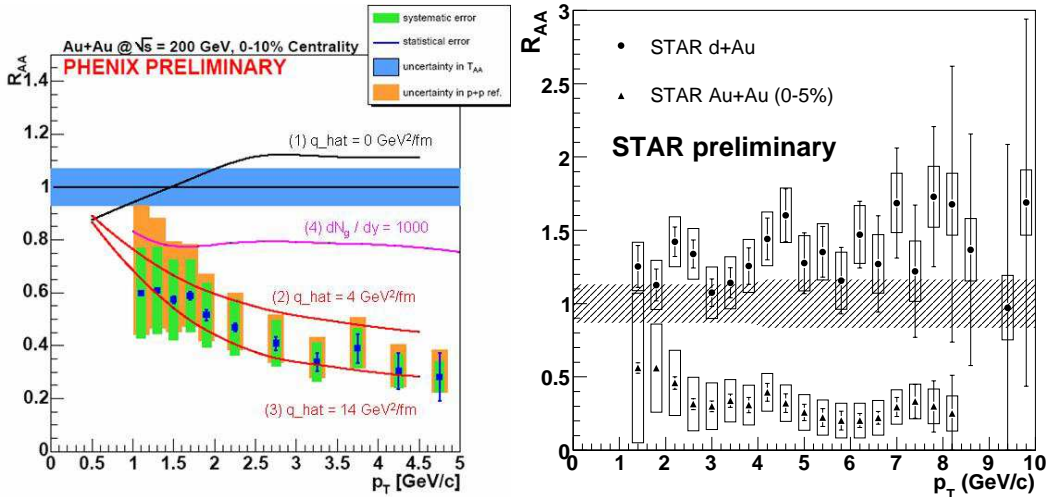


**FIGURE 13.** Left panel:  $R_{AA}$  of non-photonic electrons measured by PHENIX [36] for central Au+Au collisions at  $\sqrt{s_{NN}} = 200$  GeV. Right panel:  $R_{AA}$  of non-photonic electrons measured by STAR [7] for central Au+Au collisions at  $\sqrt{s_{NN}} = 200$  GeV.

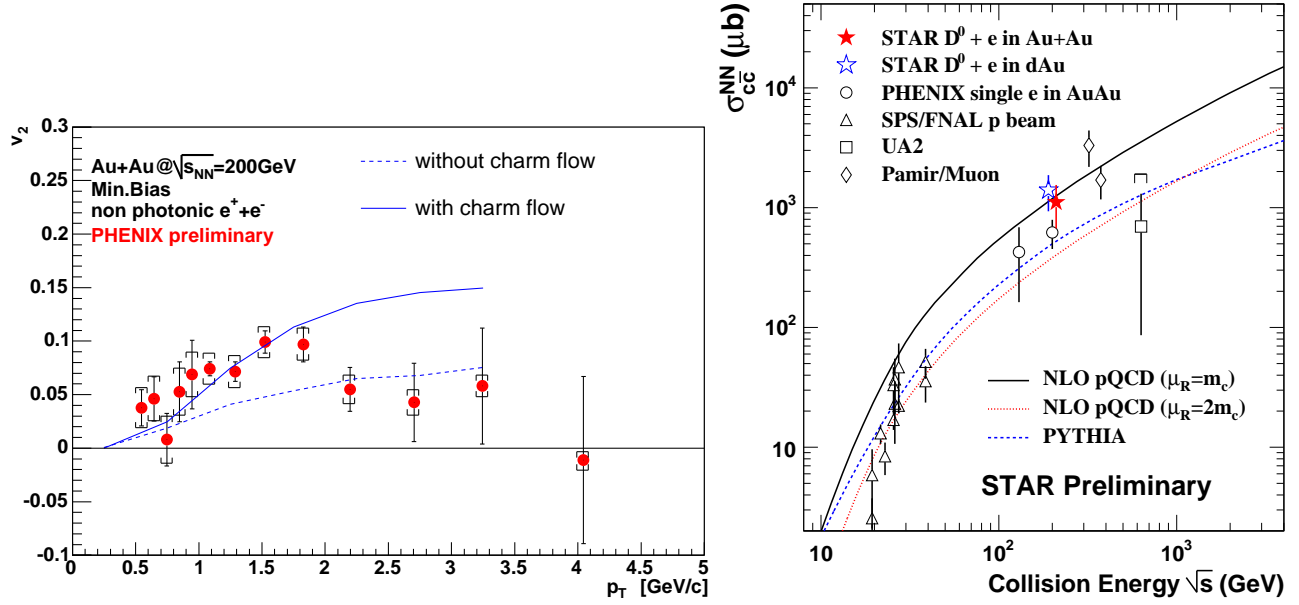


**FIGURE 14.** Left panel:  $v_2$  of non-photonic electrons attributed to semi-leptonic open charm decays measured by PHENIX [36] and compared to theoretical predictions [38]. Right panel: Compilation of the total charm cross-section production per nucleon collision  $\sigma_{cc}^{NN}$  as a function of energy compared to the NLO pQCD calculations [37].

yield is dominated by semi-leptonic decays of open charm, suggests a sizeable flow of  $D$  mesons. The comparison to calculations with and without charm flow [38] shown in Fig. 14 (left panel) favors the interpretation of charm flow. The consequence is a strong interaction with the medium and a high degree of thermalization of  $c$  quarks, favoring the strongly coupled QGP.

PHENIX has calculated the non-photonic electron measurements in  $p + p$  and minimum Au+Au collisions at  $\sqrt{s_{NN}} = 200$  GeV into a total cross-section of charm production per nucleon collision  $\sigma_{cc}^{NN}$  [39]. STAR has calculated the combined electron and direct  $D$  meson measurements in minimum bias  $d$ +Au and minimum bias Au+Au collisions [37]. There is a factor of  $\sim 2$  difference in their minimum bias Au+Au cross-sections. It is important to notice that STAR is sensitive to 80% of the total charm cross-section, while PHENIX is only sensitive to 15%. A compilation of charm cross-sections  $\sigma_{cc}^{NN}$  as a function of collision energy is displayed in Fig. 14 (right panel). Results from PHENIX and STAR are also shown.

## J/ $\psi$

PHENIX measures  $J/\psi$  in  $p + p$ ,  $d$ +Au, Cu+Cu, and Au+Au collisions at  $\sqrt{s_{NN}} = 200$  GeV and Cu+Cu at  $\sqrt{s_{NN}} = 62$  GeV at mid-pseudorapidity  $|\eta| < 0.35$  through the  $e^+e^-$  decay channel and forward pseudorapidity  $|\eta| \in [1.2, 2.2]$  through the  $\mu^+\mu^-$  decay channel [40]. The  $R_{AA}$  as a function of centrality  $N_{part}$  for the measurements at  $\sqrt{s_{NN}}$

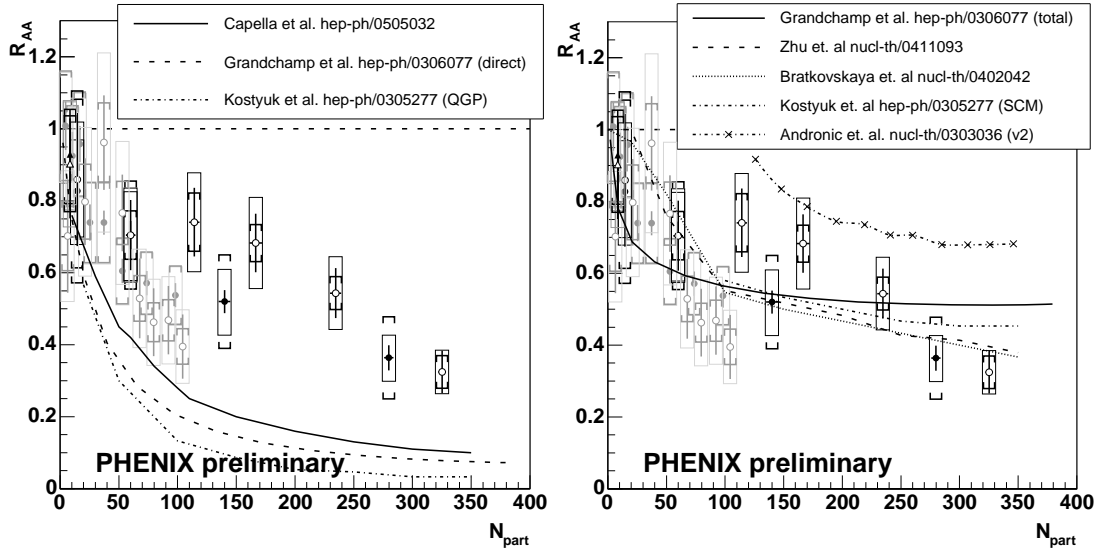


**FIGURE 15.**  $R_{AA}$  of  $J/\psi$  as a function of  $N_{part}$  in  $d+Au$ ,  $Cu+Cu$ , and  $Au+Au$  collisions at  $\sqrt{s_{NN}} = 200$  GeV measured by PHENIX. Left panel: The measurements are compared to models that explain the  $J/\psi$  NA50 anomalous suppression [42, 43, 44]. Right panel: The measurements are compared to models involving either  $J/\psi$  regeneration by quark recombination [43, 44, 45, 46] or  $J/\psi$  transport in medium [47].

$= 200$  GeV are depicted in Fig. 15. The suppression is clear and within errors it seems to be independent of the collision system. Furthermore, the magnitude of the suppression of  $\sim 3$  for the most central collisions is similar to the suppression observed at SPS [41].

The left panel of Fig. 15 shows that models that were able to explain the anomalous  $J/\psi$  suppression at the SPS and that were based on interactions with comovers [42], color screening [43], or QCD-inspired in-medium effects [44] predict a stronger suppression at RHIC.

The discrepancy seems to be resolved by invoking the regeneration of  $J/\psi$  at the later stage of the collision via recombination of  $c$  and  $\bar{c}$  quarks, which are produced more abundantly at RHIC. Several attempts that combine suppression and recombination [43, 44, 45, 46] reproduce the data reasonably well, as shown in the right panel of Fig. 15.

## LOW-MASS DI-ELECTRON

The left panel from Fig. 16 depicts the measured di-electrons pairs, the background, and the subtracted spectra with uncertainty from PHENIX [48]. The right panel of Fig. 16 shows the data compared to the hadronic cocktail [48], and to theoretical predictions [49], where the  $e^+e^-$  invariant mass spectra have been calculated using different in-medium  $\rho$  spectral functions and an expanding thermal fireball model. It is still premature for any statement, but it is definitely promising.

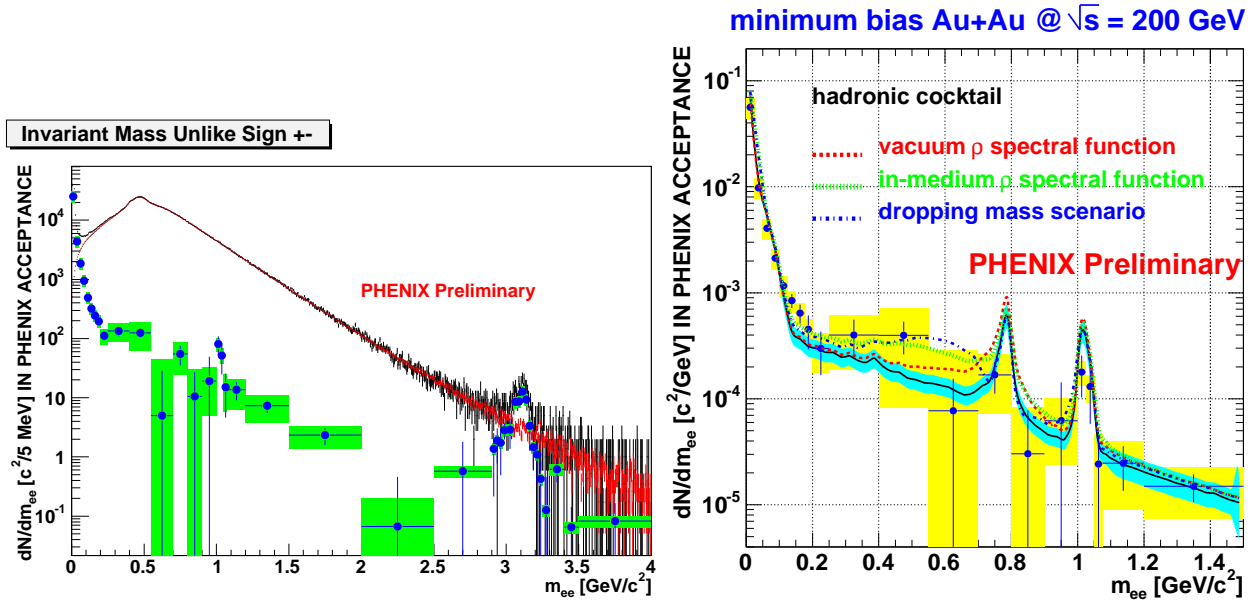


**FIGURE 16.** Left panel: The unlike sign mass spectrum together with the subtracted spectrum. Right panel: The data compared to the hadronic cocktail [48], and to theoretical predictions [49], where a  $\rho$  spectral function is introduced with and without in-medium modifications.

## SUMMARY

The baryon-meson effect observed at RHIC favors the constituent quark coalescence as the production mechanism at intermediate  $p_T$ , suggesting a partonic state prior to hadronization.  $\phi$ ,  $\Xi$ , and  $\Omega$  have small hadronic cross-sections, therefore the large  $v_2$  observed suggest that it is built up in the partonic stage. Furthermore, the thermal parameters extracted from these particles suggest that they chemically and kinetically freeze-out at the same time.

Intermediate  $p_T$  ( $p_T < 6$  GeV/c) protons behave differently than mesons at heavy-ion collisions. The large enhancement of the  $p/\pi$  ratio at intermediate  $p_T$  in Au+Au collisions indicates that jet fragmentation in vacuum is not the dominant source of particle production in this  $p_T$  range.

The suppression of high  $p_T$  hadrons in central Au + Au collisions was one of the unexpected and important phenomena observed at RHIC. The suppression is quite strong and remains approximately flat up to 20 GeV/c. Partonic radiative energy loss models [25, 26, 27] reproduce this behavior well.

The quality of the RHIC data is just marvellous, and the knowledge that this data has provided on the dense matter formed in relativistic heavy-ion collisions is without any doubt unexpected. We can only wonder how new data with new detector upgrades will surprise us.

## ACKNOWLEDGMENTS

I would like to thank F. Laue, R. Longacre, T. Ullrich, Z. Xu, and H. Zhang for the exciting discussions. This work was supported in part by the HENP Divisions of the Office of Science of the U.S. DOE.

## REFERENCES

1. P. Huovinen, nucl-th/0305064; P. Kolb, and U. Heinz, nucl-th/0305084; E. V. Shuryak, *Prog. Part. Nucl. Phys.*, **53**, 273 (2004).
2. M. Oldenburg *et. al.*, nucl-ex/0510026.
3. X. Cai *et. al.*, nucl-ex/0511004.
4. J. Adams *et. al.*, *Phys. Rev. C* **72**, 014904 (2005).
5. X. Dong *et. al.*, *Phys. Lett. B* **597**, 328 (2004).
6. J. Adams *et. al.*, *Phys. Rev. Lett.* **92**, 052302 (2004); J. Adams *et. al.*, nucl-ex/0504022.
7. J. Dunlop *et. al.*, nucl-ex/0510073.
8. D. Molnar and S. A. Voloshin, *et. al.*, *Phys. Rev. Lett.* **91**, 92301 (2003).
9. J. Adams *et. al.*, *Phys. Rev. Lett.* **92**, 112301 (2004).
10. J. Adams *et. al.*, nucl-ex/0308033.
11. L. Molnar *et. al.*, nucl-ex/0507027.
12. J. Speltz *et. al.*, nucl-ex/0512037.
13. G. Roland *et. al.*, nucl-ex/0510042.
30. V. Greene *et. al.*, QM2006 Proceedings.
15. P. Braun-Munzinger, I. Heppel, and J. Stachel *Phys. Lett. B*, **465**, 15 (1999); N. Xu and M. Kaneta, *Nucl. Phys. A* **698**, 306 (2002).
16. E. Schnedermann, J. Sollfrank, and U. W. Heinz *Phys. Rev. C*, **48**, 2462 (1993); U. A. Wiedemann and U. W. Heinz, *Phys. Rev. C* **56**, 3265 (1997).
17. J. Adams *et. al.*, *Phys. Rev. C*, **71**, 064902 (2005);
18. S. Salur *et. al.*, nucl-ex/0509036.
19. O. Barannikova *et. al.*, QM2005 Proceedings.
20. P. Staszal *et. al.*, nucl-ex/0510061.
21. M. Gyulassy, P. Levai, and I. Vitev, *Nucl. Phys. B*, **594**, 594 (2001); *Phys. Rev. D*, **66**, 014005 (2002).
22. A. Dainese, C. Loizides, and G. Paić, *Eur. Phys. J. C*, **38**, 461 (2005).
23. A. Drees, H. Feng, and J. Jia, *Phys. Rev. C*, **71**, 034909 (2005).
24. M. Shimomura *et. al.*, nucl-ex/0510023.
25. I. Vitev, *Phys. Rev. Lett.* **89**, 252301 (2002).
26. X. N. Wang, *Phys. Lett. B* **595**, 165 (2004).
27. K. Eskola *et. al.*, *Nucl. Phys. A* **747**, 511 (2005).
28. R. J. Fries *et. al.*, *Phys. Rev. Lett.* **90**, 202303 (2003); *Phys. Rev. C*, **68**, 044902 (2003).
29. R. C. Hwa and C. B. Yang, *Phys. Rev. C*, **70**, 024904 (2003).
30. V. GreKo, C. M. Ko, and P. Levai, *Phys. Rev. C*, **68**, 034904 (2003).
31. D. Magestro *et. al.*, nucl-ex/0510002.
32. I. Vitev, *Phys. Lett. B* **630**, 78 (2005).
33. J. Adams *et. al.*, *Phys. Rev. Lett.* **95**, 152301 (2005)
34. J. G. Ulery *et. al.*, nucl-ex/0510055.
35. H. Stoecker, *Nucl. Phys. A* **750**, 121 (2005); J. Casalderrey-Solana, E. V. Shuryak, and D. Teaney, hep-ph/0411314; J. Ruppert and B. Muller, *Phys. Lett. B* **618**, 123 (2005).
36. S. Butsyk *et. al.*, nucl-ex/0510010.
37. H. Zhang *et. al.*, nucl-ex/0510063.
38. V. GreKo, C. M. Ko, and R. Rapp, *Phys. Rev. Lett.*, **68**, 202 (2004).
39. S. S. Adler *et. al.*, *Phys. Rev. Lett.*, **94**, 082301 (2005).
40. H. Buesching *et. al.*, nucl-ex/0511044.
41. I. Tserruya *et. al.*, nucl-ex/0601036.

42. A. Capella and E. G. Ferreira, *Eur. Phys. J. C*, **42**, 419 (2005).
43. A. P. Kostyuk *et. al.*, *Phys. Rev. C*, **68**, 041902 (2003).
44. L. GrandChamp, R. Rapp, and G. E. Brown, *Phys. Rev. Lett.*, **92**, 212301 (2004).
45. E. L. Bratkovskaya *et. al.*, *Phys. Rev. C*, **69**, 054903 (2004).
46. A. Andronic *et. al.*, *Phys. Lett. B* **571**, 36 (2003).
47. X. L. Zhu, P.F. Zhuang, and N. Xu, *Phys. Lett. B* **607**, 107 (2005).
48. A. Toia, *et. al.*, nucl-ex/0510006.
49. R. Rapp, *Phys. Rev. C*, **63**, 054907 (2001); nucl-th/0204003.